Chiral Optical Nano-Cavity with Atomically Thin Mirrors

Daniel G. Suárez-Forero,[1, *] Ruihao Ni,[2, *] Supratik Sarkar,[1, *] Mahmoud Jalali Mehrabad,[1, *] Erik Mechtel,[1] Valery Simonyan,[1] Andrey Grankin,[1] Kenji Watanabe,[3] Takashi Taniguchi,[4] Suji Park,[5] Houk Jang,[5] Mohammad Hafezi[†,1, 6] and You Zhou[‡2, 7]

[1]*Joint Quantum Institute (JQI), University of Maryland, College Park, MD 20742, USA*
[2]*Department of Materials Science and Engineering,*
University of Maryland, College Park, MD 20742, USA
[3]*Research Center for Electronic and Optical Materials,*
National Institute for Materials Science, 1-1 Namiki, Tsukuba 305-0044, Japan
[4]*Research Center for Materials Nanoarchitectonics,*
National Institute for Materials Science, 1-1 Namiki, Tsukuba 305-0044, Japan
[5]*Center for Functional Nanomaterials, Brookhaven National Laboratory, Upton, NY 11973, USA*
[6]*Institute for Theoretical Physics, ETH Zurich, 8093 Zurich, Switzerland*
[7]*Maryland Quantum Materials Center, College Park, Maryland 20742, USA*

A fundamental requirement for photonic technologies is the ability to control the confinement and propagation of light. Widely utilized platforms include two-dimensional (2D) optical microcavities in which electromagnetic waves are confined between either metallic or multi-layer dielectric distributed Bragg reflectors. However, the fabrication complexities of thick Bragg reflectors and high losses in metallic mirrors have motivated the quest for efficient and compact mirrors. Recently, 2D transition metal dichalcogenides hosting tightly bound excitons with high optical quality have emerged as promising atomically thin mirrors. In this work, we propose and experimentally demonstrate a sub-wavelength 2D nano-cavity using two atomically thin mirrors with degenerate resonances. Remarkably, we show how the excitonic nature of the mirrors enables the formation of chiral and tunable optical modes upon the application of an external magnetic field. Moreover, temperature-dependent reflectance measurements indicate robustness and tunability up to ≈ 100 K for the device. Our work establishes a new regime for engineering intrinsically chiral sub-wavelength optical cavities and opens avenues for realizing spin-photon interfaces and exploring chiral many-body cavity electrodynamics.

The ability to confine light to small volumes is central for engineering light-matter interaction in photonic and optoelectronic technologies [1–4]. Planar microcavities are a key platform for confining the spatial extent of electromagnetic waves and manipulating the photonic density of states [5, 6], which has enabled many applications such as filtering [7], lasing [8], optical detection [9], and all-optical switching [10, 11]. In these cavities, standing optical modes form between two mirrors, which can be metallic or dielectric [12]. However, metallic mirrors suffer from intrinsically high optical losses[13], while dielectric mirrors are made of micrometric-thick heterostructures longer than the wavelength [14].

In addition to compactness and efficiency, another highly desirable feature for optical devices is chirality [15], a characteristic that emerges due to symmetry breaking. Recent research has focused on chiral coupling between light and emitters for classical and quantum optical applications, such as non-reciprocal optical routers and spin-photon interfaces. Examples include engineering polarization-selective spin-photon interfaces in photonic waveguides [16–18] and ring resonators [19–22], polaritonic chiral microcavities through magnetic [23–25] or optical [26] manipulation of an active medium hosted in the cavity, as well as realizing topological photonic states by time-reversal symmetry breaking [25].

Recently, transition metal dichalcogenides (TMDs)

have emerged as a new materials platform for exploring photon confinement and chiral light-matter coupling. In particular, strong and narrowband reflection has been demonstrated in monolayer $MoSe_2$ thanks to their high optical quality, i.e., a large ratio of radiative (Γ_r) to non-radiative (Γ_{nr}) decay rates [27, 28]. The integration of TMDs with photonic structures has also enabled several chiral phenomena, including spin-polarized excitons [29], hybrid exciton-polaritons [30, 31] and phonon-polaritons [32], by leveraging their valley-dependent optical selection rules. In these demonstrations, however, the TMDs are utilized as the active optical component instead of constituting the photonic structures [33, 34].

In this work, we propose and experimentally demonstrate a novel method for realizing nanometer-thick planar optical cavities with intrinsic chiral characteristics using two atomically thin TMD mirrors as the fundamental photonic components. In contrast to conventional Fabry–Pérot interferometric cavities, the electromagnetic mode in our system arises via the efficient optical excitation and recombination of excitons in the two TMD mirrors (Fig. 1a). Remarkably, due to the excitonic nature of the cavity's mirrors, we observe spin-polarized cavity modes that bifurcate due to the valley Zeeman effect under an external magnetic field with tunable energies. Moreover, we demonstrate the excitonic saturation of the optical mode as a function of pump power and show its

robust tunability via temperatures up to 100 K.

Device design and simulation

The realization of this cavity based on atomically thin materials relies on the high reflection from monolayer $MoSe_2$ at the excitonic resonance. In particular, an optically thin material can act as a narrow-band resonant mirror near its optical resonance. For excitons in atomically thin materials, the reflectance reaches its peak at the exciton wavelength, with a value determined by the ratio Γ_r/Γ_{nr} (see Supplementary Material). Exciton reflectances of more than 85% have been experimentally realized in $MoSe_2$, thanks to the significant oscillator strengths and relatively low non-radiative rates of the excitons in TMDs when they are encapsulated inside hexagonal boron nitride (hBN) [27, 35] (Fig. 1a). Utilizing such an effect, we can stack two monolayers vertically to form an optical cavity at the exciton wavelength with a thickness determined by the dielectric spacer (Fig. 1a and b).

The demonstration of such a conceptually simple cavity, however, imposes significant experimental challenges. Strains and disorders introduced during the assembly of van der Waals (vdW) heterostructures can not only enhance the non-radiative processes, which reduces the reflectance of the monolayer but also lead to inhomogeneous broadening and the variation of exciton energies across the samples. This makes it difficult to realize high reflectivity in both TMD monolayers while exactly matching the energies of the reflection peaks. To overcome this challenge, we first assemble a series of hBN-encapsulated monolayer $MoSe_2$ on a silicon substrate and characterize their optical response at 4 K. In doing so, we can select regions of two TMD samples with not only high exciton reflectivity but also similar exciton energy. We then transfer one heterostructure on top of the other to form the cavity. This offers a more controllable way of fabricating cavities as it involves only a single transfer step that will likely introduce less strain and disorders than the full assembly of the vdW structure.

In our experiments, we design the device such that two monolayer mirrors of MoSe2 are embedded inside layers of hBN encapsulation with a total hBN thickness of 240 nm (Fig. 1b). The monolayers are positioned symmetrically at 60 nm from the top and bottom of the vdW heterostructure (a schematic of the device is shown in Fig. 1b). The thickness of various layers is chosen based on a transfer matrix method (TMM) simulation. Importantly, we note that the TMDs separation is slightly shorter than half the wavelength of the exciton resonance (in the hBN medium). At precisely the half-wavelength condition, the standing cavity mode becomes optically dark because of the vanishing electric field at the locations of the TMDs, and can only decay by non-radiative means. This would be analogous to a Fabry-Perot cavity with finite absorption loss and zero transmission mirrors (see Supplementary Materials for additional discussion). Meanwhile, the total thickness of the hBN obeys the requirement of having minimum reflectance from the SiO_2 substrate-hBN system at the exciton resonance, which facilitates the identification of the optical mode (see Supplementary Material for a complete discussion about the role of the hBN thickness).

Figures 1c-d show the reflectance spectra of two $MoSe_2$ monolayers at 4 K, before they were stacked together to form the cavity. The reflectance spectra can be fitted using the TMM and modeling the 2D material's optical response as a Lorentz oscillator [27, 28, 36, 37], from which we extract Γ_r and Γ_{nr} (see Supplementary Material). With this information, we proceed to verify the device design using TMM and finite-difference time-domain (FDTD) simulations and extract reflectance and effective mode length (Fig. 1e see Methods for further details). The effective mode length is a measure of the distribution of the optical field, which is equal to the physical thickness of the device for non-resonant wavelengths, and becomes reduced if there is a localization of the electromagnetic field (see Supplementary Material for its mathematical definition and related discussion). The emergence of a minimum in both the reflectance and effective mode length (Fig. 1e), as well as the electric field intensity distribution (Fig. 1f) confirm the formation of a standing optical mode at a wavelength $\lambda \approx 756$ nm. FDTD simulations indicate that this optical mode has a quality factor of $Q \approx 1060$ at the resonance wavelength.In the absence of nonradiative losses, the separation between TMDs can be arbitrarily close to $\lambda/2$, with a cavity mode of an infinitely long lifetime. However, non-radiative processes lead to the disappearance of such modes. Therefore, Γ_{nr} sets the limit for how close to $\lambda/2$ the cavity length can be while still having a detectable cavity mode (Supplementary Material).

Figure 1g shows TMM simulations of the reflectance spectrum of such a vdW heterostructure for variable energy detuning between the top (X_{top}) and bottom (X_{bottom}) monolayers' excitons, using the obtained values of Γ_r and Γ_{nr} for each monolayer. For detuned resonances, the spectrum shows two individual reflectance peaks, but as one approaches degeneracy, the optical mode establishes, as highlighted by the encircled area in the figure.

Nano-cavity device characterization

A microscope picture of the final device is presented in Fig. 2a. The boundaries of hBN, top, and bottom $MoSe_2$ monolayers, are indicated in black, blue, and red, respectively. The experimental reflectance is presented in Fig. 2b (red line) along with a TMM fitting (dashed black line). The slight deviations in the final device's re-
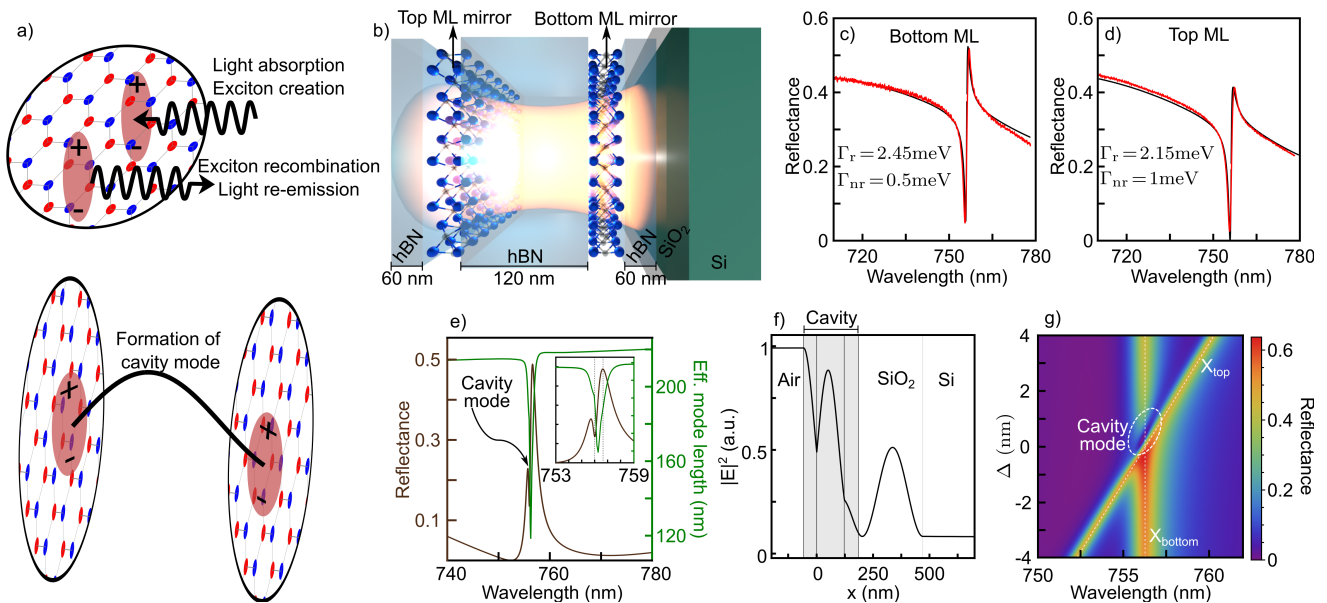
FIG. 1. Design and fabrication of a cavity based on atomically thin mirrors. a) Mechanism for the realization of a nano-cavity based on atomically thin mirrors. Upper panel: Due to the high optical quality of the exciton in the material, the monolayer (ML) effectively acts as a mirror at the resonant wavelength. Lower panel: stacking two mirrors separated by dielectric material can lead to the formation of optical modes in the structure. b) Schematic representation of the TMD nano-cavity device: two atomically thin $MoSe_2$ mirrors embedded in hBN confine the electromagnetic mode. c-d) Individual reflectance spectra of the component monolayers before stacking the final device (red). The black lines show the TMM fittings, calculated by using a Lorentz oscillator model with the decay rates indicated in each panel. e) Simulation of the device reflectance and effective mode length calculated by using TMM and FDTD simulations, respectively. The inset shows a zoom-in of the functions in a reduced range of wavelengths, with the same y-axis scales. f) Electric field intensity distribution from FDTD simulation. The minimum in both the reflectance spectrum and effective mode length (e), and enhancement of the electric field intensity profile at resonance (f) indicate the formation of a standing optical mode. g) TMM simulation of the device's spectrum upon variable exciton energy of the top monolayer X_{top}. X_{bottom} denotes the excitonic resonance of the bottom monolayer and $\Delta = X_{top} - X_{bottom}$. The formation of a cavity mode manifests as a minimum in the reflectance for the range of parameters indicated by the dashed white ellipse.

flectance spectrum from the original design might stem from the stacking of the final device, which could introduce various effects, including strain and disorder. Nevertheless, the narrow dip in the reflectance confirms the presence of the confined electromagnetic mode in the nano-cavity. Fig. 2c shows the photoluminescence (PL) spectrum of the sample at the same spot. Unlike reflectance spectra with complex lineshape, the exciton emission (X_0) is a Lorentzian peak centered at the cavity mode. In addition, a secondary peak from charged excitonic states ($X^{\pm}$) is detected at longer wavelengths, which is not resonant with the optical mode [38].

Magnetically-induced chirality

The excitonic origin of the high reflectance in the monolayer TMD mirrors endows the nano-cavity with another unique capability, i.e., a chiral behavior induced by an external magnetic field (B). To demonstrate this chirality, we measure the B-dependent reflectance when illuminating the sample with opposite circular polariza-

tion (σ^+ and σ^-) in a Faraday configuration (see Methods). Fig. 3a shows the reflectance spectra of the device for the two circular polarization states under three different values of B: 0 T, 5 T, and 10 T. The degeneracy of two optical modes with orthogonal circular polarization is lifted with increasing B. This behavior originates in the valley-dependent optical selection rule and the valley Zeeman effect of TMD monolayers due to inversion symmetry breaking and spin-orbit coupling[39, 40]: a magnetic field splits the energy of excitons in the K and -K valleys, which shift the reflectance peak and the cavity mode of σ^+ and σ^- light (in set of Fig. 3a). Such magnetic tuning of chiral light-matter coupling is usually not achievable in photonic microcavities due to the non-magnetic nature of the typical component materials [6].

To perform a quantitative analysis of the cavity's chiral behavior, we collect data over the range of 0 T to 10 T. The reflective circular dichroism (RCD), defined as $\frac{R^+ - R^-}{R^+ + R^-}$, where $R^{+(-)}$ is the reflectance of the polarization $\sigma^{+(-)}$, is shown in Fig. 3b. The chiral behavior manifests as an increasing RCD with increasing magnetic field B, which reaches a value of 0.41 at the highest mag-
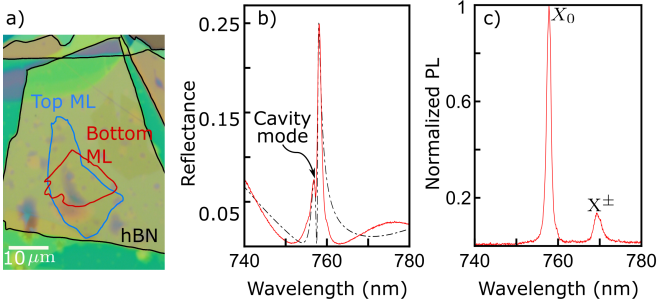
FIG. 2. Measured reflection and photoluminescence spectra of a cavity sample. a) Microscope picture of the nano-cavity device with hBN layers and $MoSe_2$ bottom and top layers indicated in black, red, and blue, respectively. b) Experimental reflectance spectrum of the device (red line) with theoretical TMM fitting (dashed black line). The confined optical mode manifests as a narrow minimum in the reflectance spectrum, as indicated by the arrow. c) PL spectrum of the device. The central emission (X_0) coincides with the device's resonant wavelength. A secondary peak from charged excitonic states is observed at longer wavelengths ($X^\pm$).

netic field of 10 T. By fitting the energy splitting of the two chiral modes in response to the magnetic field to the relationship $\Delta E = g\mu_B B$ (where μ_B is the Bohr magneton), we obtain g$= -4.46 \pm 0.45$. The extracted g-factor is in good agreement with previously reported values and theoretical predictions [33, 41, 42]. Measurements of the magnetically induced chirality performed on another spot of the sample show consistent results (see Supplementary Material).

Power and temperature dependence

We further characterize how the device's optical response is modified by optical pumping and temperatures. Fig. 4a shows the reflectance spectra of the sample when excited by a supercontinuum white laser (with a pulse duration of ≈ 1 ns) at varying power levels. The cavity mode is not significantly modified below $I_p \approx 10^{-3}$ W/μm^2. Upon further increasing the laser intensity, the mode red-shifts and broadens. Finally, above a threshold pump intensity $I_p \approx 7 \times 10^{-3}$ W/μm^2, the excitonic response and the cavity mode disappear in the reflectance spectra. The observed optical non-linearity of the cavity can originate from exciton-exciton interactions and laser-induced thermal effects. In TMD monolayers, exciton-exciton interactions produce a blueshift of the intralayer excitonic resonance, which is unlikely to be the dominant effect. Instead, laser-induced heating can introduce a redshift and additional decoherence of the excitons, which can lead to the broadening of the cavity mode as shown in the Supplementary Material, consistent with our experiments [27].

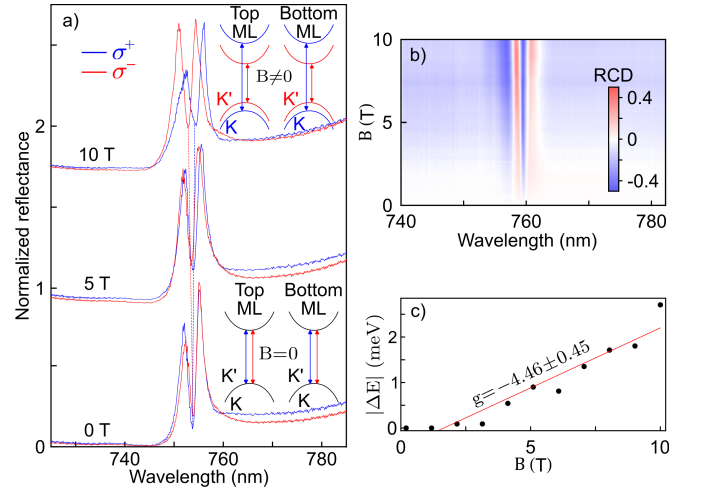We therefore further investigate the thermal effects by

FIG. 3. Chiral behavior induced by an external magnetic field B. a) Device's reflectance spectra for the orthogonal circular polarization states σ^+ (blue) and σ^- (red) at three different values of B: 0 T (bottom), 5 T (middle), and 10 T (top). The insets show a depiction of the mechanism by which the chirality is established: the modes are degenerate in the absence of a magnetic field (black scheme), but the mode split in the presence of a magnetic field and exhibits a chiral light-matter response (blue and red scheme). The data is collected at a different spot than figure 2. b) Reflective circular dichroism of the nano-cavity device for increasing B. c) Energy difference between the σ^+ and σ^- cavity modes as a function of B. A linear regression indicates a value of the magnetic factor g$= -4.46 \pm 0.45$; in good agreement with reported values and theoretical predictions.

measuring the reflectance spectra at different temperatures, as shown in Fig. 4b. We normalize the device's reflectance to that of a region without TMDs but with the same hBN thickness at each temperature. With increasing temperatures, the exciton and optical modes broaden and red-shift, in a similar fashion observed in Fig. 4a. The optical mode is robust up to a temperature $T \approx 100$ K, while the temperature tunes cavity mode over a range of ≈ 10 nm with a mode broadening of a factor ≈ 1.3. The thermal fluctuations enhance the non-radiative decay rate of the exciton by promoting the exciton-phonon decoherence, reducing the ratio Γ_r/Γ_{nr} to the critical point where the mode vanishes at $T \approx 200$ K [43, 44].

Discussion and outlook

We demonstrate a fundamentally new mechanism to achieve light confinement by harnessing the high quality of the optical excitations in TMD materials, using them as atomically thin mirrors. The 2D nature of the constituent mirrors endows this device with advantages in terms of miniaturization and integration capabilities. While our device exhibited a moderate quality factor,
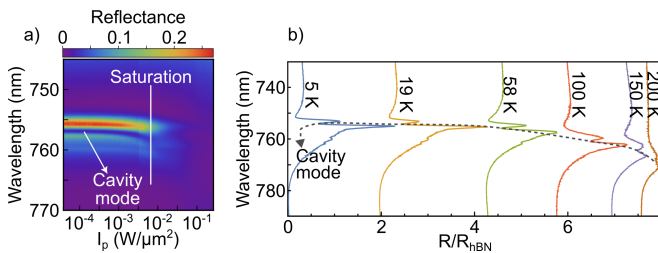
FIG. 4. Reflectance spectra of the cavity sample under different pump intensities and temperatures. a) Pump intensity-dependent reflectance spectrum. The pump intensity axis (horizontal) does not follow a linear trend, because the power was not modified linearly. As the pump power increases, the optical mode broadens due to saturation of the TMDs and thermal fluctuations, and after a critical intensity $I_p \approx 7 \times 10^{-3}$ W/μm^2, the mode completely vanishes. b) Temperature dependence of the optical mode collected with a 10^{-4} W/μm^2 white pump. The data shows a tunability of ≈ 10 nm in the range of 4 K to 100 K. At $T = 200$ K the mode is not identifiable anymore. The dashed arrow serves as a guide for the eye to track the modification of the optical mode.

future improvements in the materials' quality and heterostructure fabrication could further reduce their optical loss by decreasing the non-radiative and inhomogeneous broadening associated with disorders.

Remarkably, these cavities display unique dispersion distinct from conventional planar cavities with weak angular dependence of the resonant mode energy (see Supplementary Material Fig. S9). The weak dispersion of such a cavity can enable the efficient control of point emitters without complicated photonic structures such as photonic crystals and curved mirrors. Furthermore, such a concept can be extended to other resonant optical effects in not only 2D materials (including other TMDs and hBN [45]) but also other optically thin systems, which could enable a wide range of optical applications covering visible and IR spectra.

This platform offers exciting new ways for fabricating optical routers and filters, engineering quantum materials via its unique capability of achieving chiral light-matter coupling [16, 46–48], and realizing non-reciprocal collective super- and sub-radiant states [15, 49–51]. It is also suited for the exploration of the topological interplay between electrons and photons, such as vorticity-selective manipulation of topological electronic states [52]. The electrical and strain tuning [53–55] (in an open cavity) of the exciton resonance could enable dynamic control of the cavity mode and their chiral coupling for devices such as tunable optical isolators and polarization-dependent light-microwave transduction [56, 57]. Furthermore, optically pumping of the valley polarization in TMDs opens up the intriguing possibility of ultrafast optical control of the chiral light-matter coupling [30, 58–61]. Finally, motivated by recent observations of strongly interacting excitons in hetero-bilayer TMDs superlattice structures

[62–64], one can envisage embedding such lattices inside our planar cavity and explore the rich physics of Bose-Hubbard polaritonic models [65, 66].

Methods

TMM and FDTD numerical simulations: For the numerical simulations of the device's reflectance, we apply the transfer matrix method (TMM), by using the refractive indices of the different materials from a database. In this formalism, we simulate the response of the system to an incoming plane wave at any angle, which in this case was chosen to be $0°$. The angular dependence of the reflectance is presented and discussed in the Supplementary Material. For the calculation of the electric field intensity profile, effective cavity mode length, and Q factor, we rely on a finite-difference time-domain (FDTD) simulation implemented in commercial software. We simulate the situations of the cavity excited through an embedded dipole source, or by an incident plane wave.

Device fabrication: Monolayer MoSe$_2$ and hBN flakes were exfoliated from bulk crystals on top of silicon substrates with an oxide layer of 285 nm. High optical quality monolayers of MoSe$_2$ were obtained using the QPress Exfoliator at CFN in Brookhaven National Lab. The MoSe$_2$ flakes were identified under an optical microscope and confirmed by photoluminescence measurements. The thickness of hBN flakes was verified by atomic force microscopy. The device was assembled by the van der Waals dry transfer technique. We first fabricate several hBN/MoSe$_2$/hBN heterostructures and characterize them by photoluminescence and reflectance measurements to find the ideal spot. Finally, to obtain the nano-cavity device, two heterostructures with identical excitonic energies and high radiative decay rates were carefully chosen and stacked together.

Setup for optical measurements: The sample is held at a temperature of 6 K in a closed-loop cryostat. For the optical measurements, we use a confocal microscopy setup in reflectance configuration. The focused laser spot on the sample is about 1 μm in diameter. A tungsten lamp and a supercontinuum white laser are employed as broadband light sources; there is no difference in the results obtained with each source. For photoluminescence measurements, we use a HeNe laser (≈ 633 nm) to excite the material. For the measurements of the magnetic field dependence, polarization-resolved reflectance spectra were collected by placing a quarter-wave plate followed by a linear polarizer in the detection path. The signal is finally collected by a charge-coupled device attached to a spectrometer. A detailed description of this setup can be found in Ref. [67].

Acknowledgements

[†] hafezi@umd.edu
[‡] youzhou@umd.edu

———————

[*] These authors contributed equally to this work

[1] J. L. O'brien, A. Furusawa, and J. Vučković, Photonic quantum technologies, Nature Photonics **3**, 687 (2009).

[2] I. Carusotto and C. Ciuti, Quantum fluids of light, Reviews of Modern Physics **85**, 299 (2013), arXiv:2211.10980.

[3] D. E. Chang, V. Vuletić, and M. D. Lukin, Quantum nonlinear optics—photon by photon, Nature Photonics **8**, 685 (2014).

[4] J. Bloch, A. Cavalleri, V. Galitski, M. Hafezi, and A. Rubio, Strongly correlated electron–photon systems, Nature **606**, 41 (2022).

[5] K. J. Vahala, Optical microcavities, Nature 2003 424:6950 **424**, 839 (2003).

[6] H. Megahd, D. Comoretto, and P. Lova, (invited)planar microcavities: Materials and processing for light control, Optical Materials: X **13**, 100130 (2022).

[7] F. Monifi, Şahin Kaya Özdemir, and L. Yang, Tunable add-drop filter using an active whispering gallery mode microcavity, Applied Physics Letters **103**, 181103 (2013).

[8] R. Michalzik, Vcsel fundamentals, Springer Series in Optical Sciences **166**, 19 (2013).

[9] M. Furchi, A. Urich, A. Pospischil, G. Lilley, K. Unterrainer, H. Detz, P. Klang, A. M. Andrews, W. Schrenk, G. Strasser, and T. Mueller, Microcavity-integrated graphene photodetector, Nano Letters **12**, 2773 (2012).

[10] G. Ma, J. Shen, Z. Zhang, Z. Hua, and S. H. Tang, Ultrafast all-optical switching in one-dimensional photonic crystal with two defects, Optics Express **14**, 858 (2006).

[11] H. Nakamura, Y. Sugimoto, K. Kanamoto, N. Ikeda, Y. Tanaka, Y. Nakamura, S. Ohkouchi, Y. Watanabe, K. Inoue, H. Ishikawa, and K. Asakawa, Ultra-fast photonic crystal/quantum dot alloptical switch for future photonic networks, Optics Express **12**, 6606 (2004).

[12] A. Kavokin, J. J. Baumberg, G. Malpuech, and F. P. Laussy, *Microcavities*, 2nd ed. (Oxford Science, 2008).

[13] H. Benisty, H. D. Neve, and C. Weisbuch, Impact of planar microcavity effects on light extraction - part i: Basic concepts and analytical trends, IEEE Journal of Quantum Electronics **34**, 1612 (1998).

[14] J. D. Joannopoulos, S. G. Johnson, J. N. Winn, and R. D. Meade, *Photonic Crystals: Molding the Flow of Light (Second Edition)*, 2nd ed. (Princeton University Press, 2011).

[15] P. Lodahl, S. Mahmoodian, S. Stobbe, A. Rauschenbeutel, P. Schneeweiss, J. Volz, H. Pichler, and P. Zoller, Chiral quantum optics, Nature **541**, 473 (2017).

[16] I. Söllner, S. Mahmoodian, S. L. Hansen, L. Midolo, A. Javadi, G. Kiršanskė, T. Pregnolato, H. El-Ella, E. H. Lee, J. D. Song, *et al.*, Deterministic photon–emitter coupling in chiral photonic circuits, Nature nanotechnology **10**, 775 (2015).

[17] S. Barik, A. Karasahin, C. Flower, T. Cai, H. Miyake, W. DeGottardi, M. Hafezi, and E. Waks, A topological quantum optics interface, Science **359**, 666 (2018).

[18] M. J. Mehrabad, S. Mittal, and M. Hafezi, Topological photonics: fundamental concepts, recent developments, and future directions (2023), arXiv:2305.16528 [physics.optics].

[19] S. Barik, A. Karasahin, S. Mittal, E. Waks, and M. Hafezi, Chiral quantum optics using a topological resonator, Physical Review B **101**, 205303 (2020).

[20] M. Jalali Mehrabad, A. Foster, R. Dost, E. Clarke, P. Patil, I. Farrer, J. Heffernan, M. Skolnick, and L. Wilson, A semiconductor topological photonic ring resonator, Applied Physics Letters **116** (2020).

[21] M. J. Mehrabad, A. P. Foster, R. Dost, E. Clarke, P. K. Patil, A. M. Fox, M. S. Skolnick, and L. R. Wilson, Chiral topological photonics with an embedded quantum emitter, Optica **7**, 1690 (2020).

[22] M. J. Mehrabad, A. Foster, N. Martin, R. Dost, E. Clarke, P. Patil, M. Skolnick, and L. Wilson, Chiral topological add–drop filter for integrated quantum photonic circuits, Optica **10**, 415 (2023).

[23] T. P. Lyons, D. J. Gillard, C. Leblanc, J. Puebla, D. D. Solnyshkov, L. Klompmaker, I. A. Akimov, C. Louca, P. Muduli, A. Genco, M. Bayer, Y. Otani, G. Malpuech, and A. I. Tartakovskii, Giant effective Zeeman splitting in a monolayer semiconductor realized by spin-selective strong light–matter coupling, Nature Photonics 2022 16:9 **16**, 632 (2022).

[24] D. G. Suárez-Forero, D. W. Session, M. Jalali Mehrabad, P. Knüppel, S. Faelt, W. Wegscheider, and M. Hafezi, Spin-selective strong light–matter coupling in a 2D hole gas-microcavity system, Nature Photonics 2023 , 1 (2023).

[25] S. Klembt, T. Harder, O. Egorov, K. Winkler, R. Ge, M. Bandres, M. Emmerling, L. Worschech, T. Liew, M. Segev, *et al.*, Exciton-polariton topological insulator, Nature **562**, 552 (2018).

[26] N. Carlon Zambon, P. St-Jean, M. Milićević, A. Lemaître, A. Harouri, L. Le Gratiet, O. Bleu, D. Solnyshkov, G. Malpuech, I. Sagnes, *et al.*, Optically controlling the emission chirality of microlasers, Nature Photonics **13**, 283 (2019).

[27] G. Scuri, Y. Zhou, A. A. High, D. S. Wild, C. Shu, K. D. Greve, L. A. Jauregui, T. Taniguchi, K. Watanabe, P. Kim, M. D. Lukin, and H. Park, Large excitonic

reflectivity of monolayer mose2 encapsulated in hexagonal boron nitride, Physical Review Letters **120**, 037402 (2018).

[28] P. Back, S. Zeytinoglu, A. Ijaz, M. Kroner, and A. Imamoğlu, Realization of an electrically tunable narrow-bandwidth atomically thin mirror using monolayer mose2, Physical Review Letters **120**, 037401 (2018).

[29] R. Shreiner, K. Hao, A. Butcher, and A. A. High, Electrically controllable chirality in a nanophotonic interface with a two-dimensional semiconductor, Nature Photonics **16**, 330 (2022).

[30] W. Liu, Z. Ji, Y. Wang, G. Modi, M. Hwang, B. Zheng, V. J. Sorger, A. Pan, and R. Agarwal, Generation of helical topological exciton-polaritons, Science **370**, 600 (2020).

[31] M. Li, I. Sinev, F. Benimetskiy, T. Ivanova, E. Khestanova, S. Kiriushechkina, A. Vakulenko, S. Guddala, M. Skolnick, V. M. Menon, *et al.*, Experimental observation of topological z2 exciton-polaritons in transition metal dichalcogenide monolayers, Nature communications **12**, 4425 (2021).

[32] S. Guddala, F. Komissarenko, S. Kiriushechkina, A. Vakulenko, M. Li, V. Menon, A. Alù, and A. Khanikaev, Topological phonon-polariton funneling in midinfrared metasurfaces, Science **374**, 225 (2021).

[33] A. Srivastava, M. Sidler, A. V. Allain, D. S. Lembke, A. Kis, and A. Imamoglu, Valley zeeman effect in elementary optical excitations of monolayer wse2, Nature Physics **11**, 141 (2015).

[34] X. Xu, W. Yao, D. Xiao, and T. F. Heinz, Spin and pseudospins in layered transition metal dichalcogenides, Nature Physics **10**, 343 (2014).

[35] F. Cadiz, E. Courtade, C. Robert, G. Wang, Y. Shen, H. Cai, T. Taniguchi, K. Watanabe, H. Carrere, D. Lagarde, *et al.*, Excitonic linewidth approaching the homogeneous limit in mos 2-based van der waals heterostructures, Physical Review X **7**, 021026 (2017).

[36] P. Y. Yu and M. Cardona, *Fundamentals of Semiconductors*, 4th ed. (Springer, 2010) pp. 345–426.

[37] M. M. Glazov, T. Amand, X. Marie, D. Lagarde, L. Bouet, and B. Urbaszek, Exciton fine structure and spin decoherence in monolayers of transition metal dichalcogenides, Physical Review B - Condensed Matter and Materials Physics **89**, 201302 (2014).

[38] G. D. Shepard, J. V. Ardelean, O. A. Ajayi, D. Rhodes, X. Zhu, J. C. Hone, and S. Strauf, Trion-Species-Resolved Quantum Beats in MoSe2, ACS Nano **11**, 11550 (2017).

[39] D. Xiao, G. B. Liu, W. Feng, X. Xu, and W. Yao, Coupled spin and valley physics in monolayers of MoS 2 and other group-VI dichalcogenides, Physical Review Letters **108**, 196802 (2012).

[40] F. Xuan and S. Y. Quek, Valley Zeeman effect and Landau levels in two-dimensional transition metal dichalcogenides, Physical Review Research **2**, 033256 (2020).

[41] G. Aivazian, Z. Gong, A. M. Jones, R.-L. Chu, J. Yan, D. G. Mandrus, C. Zhang, D. Cobden, W. Yao, and X. Xu, Magnetic control of valley pseudospin in monolayer wse$_2$, Nature Physics **11**, 148 (2015).

[42] C. Robert, H. Dery, L. Ren, D. Van Tuan, E. Courtade, M. Yang, B. Urbaszek, D. Lagarde, K. Watanabe, T. Taniguchi, *et al.*, Measurement of conduction and valence bands g-factors in a transition metal dichalcogenide monolayer, Physical Review Letters **126**, 067403 (2021).

[43] T. Jakubczyk, K. Nogajewski, M. R. Molas, M. Bartos, W. Langbein, M. Potemski, and J. Kasprzak, Impact of environment on dynamics of exciton complexes in a ws$_2$ monolayer, 2D Materials **5**, 031007 (2018).

[44] I. Epstein, B. Terrés, A. J. Chaves, V.-V. Pusapati, D. A. Rhodes, B. Frank, V. Zimmermann, Y. Qin, K. Watanabe, T. Taniguchi, H. Giessen, S. Tongay, J. C. Hone, N. M. R. Peres, and F. H. L. Koppens, Near-unity light absorption in a monolayer ws$_2$ van der waals heterostructure cavity, Nano Letters **20**, 3545 (2020).

[45] E. Y. Ma, J. Hu, L. Waldecker, K. Watanabe, T. Taniguchi, F. Liu, and T. F. Heinz, The reststrahlen effect in the optically thin limit: A framework for resonant response in thin media, Nano Letters **22**, 8389 (2022).

[46] H. Hübener, U. De Giovannini, C. Schäfer, J. Andberger, M. Ruggenthaler, J. Faist, and A. Rubio, Engineering quantum materials with chiral optical cavities, Nature Materials 2020 20:4 **20**, 438 (2020).

[47] C. Jiang, M. Baggioli, and Q.-D. Jiang, Engineering flat bands in twisted-bilayer graphene away from the magic angle with chiral optical cavities, arXiv:2306.05149 (2023).

[48] D. L. Hurst, D. M. Price, C. Bentham, M. N. Makhonin, B. Royall, E. Clarke, P. Kok, L. R. Wilson, M. S. Skolnick, and A. M. Fox, Nonreciprocal transmission and reflection of a chirally coupled quantum dot, Nano Letters **18**, 5475 (2018).

[49] P. O. Guimond, A. Grankin, D. V. Vasilyev, B. Vermersch, and P. Zoller, Subradiant bell states in distant atomic arrays, Physical Review Letters **122**, 093601 (2019).

[50] W. Langbein, C. Mann, U. Woggon, M. Klude, and D. Hommel, Radiative coupling of excitons in ZnSe double quantum wells, Physica status solidi (a) **190**, 861 (2002).

[51] S. Haas, T. Stroucken, M. Hübner, J. Kuhl, B. Grote, A. Knorr, F. Jahnke, S. W. Koch, R. Hey, and K. Ploog, Intensity dependence of superradiant emission from radiatively coupled excitons in multiple-quantum-well bragg structures, Physical Review B **57**, 14860 (1998).

[52] D. Session, M. J. Mehrabad, N. Paithanker, T. Grass, C. Eckhardt, B. Cao, D. G. S. Forero, K. Li, M. S. Alam, G. S. Solomon, N. Schine, J. Sau, R. Sordan, and M. Hafezi, Optical pumping of electronic quantum hall states with vortex light (2023), arXiv:2306.03417.

[53] K. F. Mak, K. He, C. Lee, G. H. Lee, J. Hone, T. F. Heinz, and J. Shan, Tightly bound trions in monolayer MoS2, Nature Materials **12**, 207 (2012).

[54] J. S. Ross, S. Wu, H. Yu, N. J. Ghimire, A. M. Jones, G. Aivazian, J. Yan, D. G. Mandrus, D. Xiao, W. Yao, and X. Xu, Electrical control of neutral and charged excitons in a monolayer semiconductor, Nature Communications **4**, 1 (2013).

[55] M. Sidler, P. Back, O. Cotlet, A. Srivastava, T. Fink, M. Kroner, E. Demler, and A. Imamoglu, Fermi polaron-polaritons in charge-tunable atomically thin semiconductors, Nature Physics **13**, 255 (2016).

[56] Y. Zhou, G. Scuri, J. Sung, R. Gelly, D. Wild, K. D. Greve, A. Joe, T. Taniguchi, K. Watanabe, P. Kim, M. Lukin, and H. Park, Controlling excitons in an atomically thin membrane with a mirror, Physical Review Letters **124** (2020).

[57] X. Gao, Z.-Q. Yin, and T. Li, High-speed quantum transducer with a single-photon emitter in a 2d resonator, Annalen der Physik **532**, 2000233 (2020).

[58] S. Guddala, Y. Kawaguchi, F. Komissarenko, S. Kiriushechkina, A. Vakulenko, K. Chen, A. Alù, V. M. Menon, and A. B. Khanikaev, All-optical nonreciprocity due to valley polarization pumping in transition metal dichalcogenides, Nature Communications **12**, 10.1038/s41467-021-24138-0 (2021).

[59] Z. Sun, J. Gu, A. Ghazaryan, Z. Shotan, C. R. Considine, M. Dollar, B. Chakraborty, X. Liu, P. Ghaemi, S. Kéna-Cohen, and V. M. Menon, Optical control of room-temperature valley polaritons, Nature Photonics **11**, 491 (2017).

[60] K. Hao, R. Shreiner, A. Kindseth, and A. A. High, Optically controllable magnetism in atomically thin semiconductors, Science Advances **8** (2022).

[61] G. Wang, A. Chernikov, M. M. Glazov, T. F. Heinz, X. Marie, T. Amand, and B. Urbaszek, Colloquium: Excitons in atomically thin transition metal dichalcogenides, Reviews of Modern Physics **90** (2018).

[62] R. Xiong, J. H. Nie, S. L. Brantly, P. Hays, R. Sailus, K. Watanabe, T. Taniguchi, S. Tongay, and C. Jin, Correlated insulator of excitons in wse2/ws2 moiré superlattices, Science **380**, 860 (2023).

[63] H. Park, J. Zhu, X. Wang, Y. Wang, W. Holtzmann, T. Taniguchi, K. Watanabe, J. Yan, L. Fu, T. Cao, *et al.*, Dipole ladders with large hubbard interaction in a moiré exciton lattice, Nature Physics , 1 (2023).

[64] B. Gao, D. G. Suárez-Forero, S. Sarkar, T.-S. Huang, D. Session, M. J. Mehrabad, R. Ni, M. Xie, J. Vannucci, S. Mittal, *et al.*, Excitonic mott insulator in a bose-fermi-hubbard system of moiré ws_2/wse_2 heterobilayer, arXiv:2304.09731 (2023).

[65] D. G. Angelakis, Quantum simulations with photons and polaritons, Quantum Science and Technology (Springer, 2017) **134** (2017).

[66] M. J. Hartmann, Quantum simulation with interacting photons, Journal of Optics **18**, 104005 (2016).

[67] J. C. Sell, J. R. Vannucci, D. G. Suárez-Forero, B. Cao, D. W. Session, H.-J. Chuang, K. M. Mccreary, M. R. Rosenberger, B. T. Jonker, S. Mittal, and M. Hafezi, Magneto-optical measurements of the negatively charged $2s$ exciton in WSe_2, Physical Review B **106**, 81409 (2022).

[68] E. D. Palik, *Handbook of Optical Constants of Solids* (Elsevier, 1985).

Supplementary Material

I. MODELING A TMD MONOLAYER AS A LORENTZ OSCILLATOR

The strong modulation of the refractive index of a TMD monolayer upon driving the excitonic resonance can be well described by a Lorentz oscillator model. By fitting the reflectance spectrum of each monolayer-hBN heterostructure (before stacking) to such a model, using a Transfer Matrix Method (TMM) formalism (as described in the Methods Section), we extract the real and imaginary parts of the refractive indices of the top and bottom monolayers. We also use the decay parameters of the TMD mirror reported by Scuri *et al.* in Ref. [27] to estimate the performance of a device made with two such monolayers. We use their parameters as they reported a monolayer with the best optical quality and highest reflectance. This anticipates what one can expect from a TMD cavity made of monolayers of superior optical quality. In this theoretical formalism, the susceptibility of the TMD monolayer is given by

$$\chi(\omega) = -\frac{c}{\omega_0 d} \frac{\Gamma_r}{(\omega - \omega_0) + i\Gamma_{nr}/2}, \qquad \text{(S1)}$$

where ω_0 is the excitonic resonance frequency, d (= 0.7 nm) is the thickness of a TMD monolayer, and Γ_r and Γ_{nr} are the radiative and non-radiative decay rates, respectively. Γ_r is the rate at which an exciton in the monolayer recombines by emitting a photon, whereas, Γ_{nr} is the non-radiative recombination rate via processes such as phonon scattering. The frequency-dependent complex refractive index of the TMD monolayer is then

$$n_{\text{TMD}}(\omega) = \sqrt{n_{\text{bulk}}^2(\omega) - \frac{c}{\omega_0 d} \frac{\Gamma_r}{(\omega - \omega_0) + i\Gamma_{nr}/2}}, \qquad \text{(S2)}$$

where n_{bulk} is the refractive index of the bulk TMD material (and hence without the excitonic resonance).

From the fittings (as shown in Fig. 1 in the main text) we obtain the following values:
Top monolayer: $\Gamma_r = 2.45$ meV, $\Gamma_{nr} = 0.5$ meV, $\lambda_0 = 756.2$ nm.
Bottom monolayer: $\Gamma_r = 2.15$ meV, $\Gamma_{nr} = 1$ meV, $\lambda_0 = 756.2$ nm.
For comparison, the decay rates of the monolayer reported in Scuri *et al.* are [27]: $\Gamma_r = 4.38$ meV, $\Gamma_{nr} = 0.2$ meV.
Although the resonant wavelength of the monolayer TMD mirror demonstrated in Scuri *et al.* differs from our two monolayers, for theoretical comparison purposes, we assume it has the same resonance wavelength, i.e., $\lambda_0 = 756.2$ nm. In the following sections, we use the obtained refractive indices of the aforementioned three monolayers to study different cavity geometries. For the TMM and FDTD simulations, we use the refractive indices obtained from Ref. [68], which at the exciton resonance wavelength correspond to $n_{\text{hBN}}(756.2$ nm$) \approx 2.1$, $n_{\text{SiO}_2}(756.2$ nm$) \approx 1.5$, $n_{\text{Si}}(756.2$ nm$) \approx 3.7$.

II. A $\lambda_0/2$ CAVITY

In the most simplistic scenario, one can imagine a cavity formed by two TMD monolayers separated by air. From the physics of Fabry-Perot cavities, we intuitively expect to have the best optical confinement when the spacing between the TMD monolayers is an integer factor of half of the exciton resonance wavelength λ_0 because at this energy the reflectivity from the TMD is maximized. In Fig. S1a, we simulate the spectral reflectance R for different cavity thicknesses. For our simulations, we consider the excitonic resonance measured for the individual monolayers ($\lambda_0 = 756.2$ nm), and decay constants $\Gamma_r = 4.38$ meV, and $\Gamma_{nr} = 0.2$ meV. The figure shows an intriguing dependence of the confined mode for variable cavity thickness: the linewidth reduces as one approaches the condition of $\lambda_0/2 \approx 378.1$ nm (marked with a white dashed line). Generally, the energy of the mode is set by the TMD separation, while its quality factor is determined by Γ_{nr} and the reflectivity (which is maximum at the exciton resonance). Interestingly, as one approaches the $n\lambda/2$ condition (with $n \in \mathbb{N}$), the mode becomes optically inaccessible. This can be understood in terms of the mode's radiative lifetime: for a TMD cavity with mirrors separated by $n\lambda/2$, the radiative lifetime is maximum and hence, a small Γ_{nr} is enough to completely dampen the confined light. Therefore, this dark cavity mode is completely decoupled from the external electromagnetic fields, making it impossible to probe with an external source [49].

In this context, the disappearance of the cavity mode from the reflectance spectrum is expected to be independent of Γ_{nr} when the thickness of the cavity is exactly $\lambda_0/2$, as observed in Fig. S1b. This is similar to an uncommon Fabry-Perot cavity with non-zero absorption and zero transmission. For our system, this particular behavior originates in the excitonic nature of the mirrors. For this reason, regardless of the non-radiative losses in the material, the mode will be optically dark at the $\lambda_0/2$ separation. This analysis was used to engineer the cavity thickness, making it slightly different from $\lambda_0/2$ to probe the cavity mode externally, as shown in the main text.
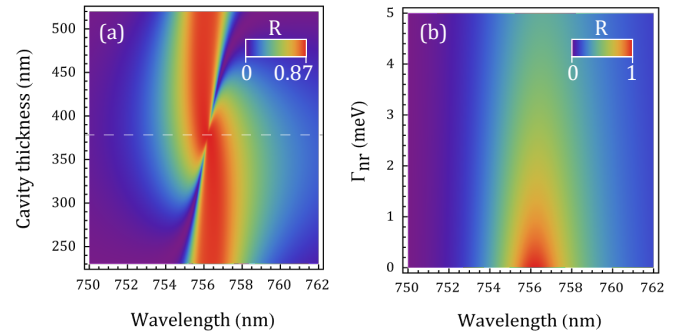

FIG. S1. (a) Reflectance of a cavity formed by two TMD monolayers ($\lambda_0 = 756.2$ nm, $\Gamma_r = 4.38$ meV, $\Gamma_{nr} = 0.2$ meV) in air for different cavity thickness. The mode is not visible in the reflectance spectrum when the thickness of the cavity is exactly $\lambda_0/2$, as marked by the white dashed line. (b) Reflectance of the cavity for varying Γ_{nr} and a cavity thickness of $\lambda_0/2$.
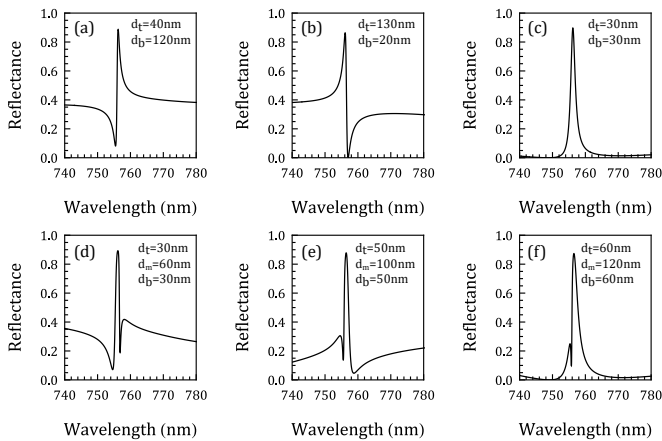
FIG. S2. a-c: Effect of the thickness of the encapsulating hBN on the reflectance of a TMD monolayer. The thicknesses of the (top, bottom) layer of hBN encapsulations are (a) (40 nm, 120 nm), (b) (130 nm, 20 nm), and (c) (30 nm, 30 nm). Different thicknesses of hBN lead to different reflectance spectra for the same monolayer. d-f: Effect of the thickness of hBN on the reflectance of the cavity heterostructure. The thickness of the (top, middle, bottom) layers of hBN used for the simulations are (d) (30 nm, 60 nm, 30 nm), (e) (50 nm, 100 nm, 50 nm), and (f) (60 nm, 120 nm, 60 nm). The best cavity mode is obtained for the parameters of panel f, which are the nominal thicknesses of the final fabricated device.

III. ROLE OF THE hBN THICKNESS

The thickness of hBN plays a crucial role in the reflectance spectrum of both a TMD monolayer and the cavity heterostructure due to the interference of light from TMD and the background. To investigate the effect of hBN thickness on monolayer devices, we simulate three scenarios with different thicknesses of the top (d_t) and bottom (d_b) hBN encapsulations in an hBN/TMD/hBN heterostructure stacked on a Si substrate with 285 nm SiO$_2$, as used in experiments. In our simulations, we consider an excitonic resonance at 756.2 nm, and decay constants $\Gamma_r = 4.38$ meV, and $\Gamma_{nr} = 0.2$ meV. As shown in Fig. S2(a-c), depending on the thickness of hBN, the sample reflectance spectra can have different Fano-lineshapes or a reflectance peak. For the stacking of the cavity device, we chose the hBN thickness such that the exciton resonance manifests as a simple reflectance peak to avoid the complex lineshape and facilitate the identification and characterization of the optical confined mode.

Next, we simulate the effect of hBN thickness on the reflectance spectrum of a cavity formed by stacking two monolayers on a similar substrate. The results of the simulations are shown in Fig. S2(d-f). Once again, we observe that different thicknesses of the top (d_t), middle (d_m), and bottom (d_b) hBN can drastically alter the reflectance spectrum of the cavity. The calculated reflectance spectra of samples with our designed device structures have minimal reflectance from the hBN around the cavity resonance frequency, as shown in panel f, making the cavity mode clearly identifiable.

From Fig. S2 we can conclude that the total thickness of hBN in the heterostructure, i.e., $d_t + d_m + d_b$, dictates the shape of the reflection spectrum. However, the distribution of the thickness of hBN is also crucial for the observation of

the cavity mode. To see that, we fix the total thickness of hBN to 240 nm, and simulate different scenarios, as shown in Fig. S3. Interestingly, one can always observe the cavity mode in reflectance except in the scenario when the spacing between the two TMD monolayers is exactly half of the wavelength of the excitonic resonance in hBN, i.e., $d_m = \lambda_0/2n_{hBN} \approx 180$ nm, where $n_{hBN} \approx 2.1$ is the refractive index of hBN at the resonance frequency. As discussed above, this happens because the electric field intensity of the cavity mode is zero at the position of the TMDs when d_m is exactly equal to $\lambda_0/2n$.
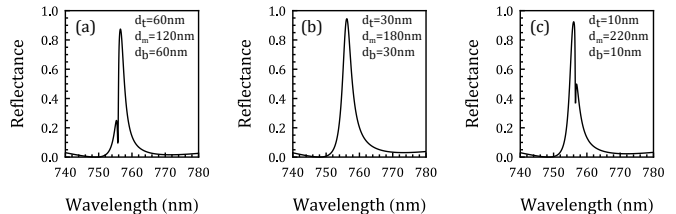

FIG. S3. Effect of the distribution of thickness of hBN on the detection of the cavity mode in reflection. The thicknesses of the (top, middle, and bottom) layers of hBN used for the simulations are (a) (60 nm, 120 nm, 60 nm), (b) (30 nm, 180 nm, 30 nm), and (c) (10 nm, 220 nm, 10 nm) such that the total thickness of hBN is always 240 nm. When the MLs are separated a distance $d_m = \lambda/2n_{hBN} \approx 180$ nm, the cavity mode is decoupled from the external field, making its detection impossible.

IV. INTERPLAY BETWEEN Γ_r AND Γ_{nr}

The radiative (Γ_r) and non-radiative (Γ_{nr}) decay rates determine the peak reflectance of a monolayer, critically affecting its spectrum. Fig. S4 shows how Γ_r and Γ_{nr} determine the absolute reflectance of the monolayer, i.e., the quality of the mirror. In panel a, we use a fixed radiative decay rate of $\Gamma_r = 4.38$ meV and vary the non-radiative decay rate. We observe that the monolayer acts as a better mirror if it has lower values of Γ_{nr}. At high values of Γ_{nr}, we only observe the absorption dip, and the reflectance peak almost disappears. Intuitively, with increasing nonradiative rates, the amount of light lost via non-radiative processes increases, which decreases the sample reflectance. This leads to the disappearance of the reflectance peak at higher values of Γ_{nr}.

Panel b shows the case where the value of Γ_{nr} is fixed to 0.2 eV and Γ_r varies. Once again, we observe that with increasing Γ_r the peak reflectance increases and broadens. This can be understood as a reduction of the exciton lifetime (but the recombination is always radiative).

Finally in panel c, both Γ_r and Γ_{nr} are varied, but the ratio Γ_r/Γ_{nr} is kept constant. In this case, the maximum and minimum value of reflectance of the TMD monolayer is constant and only the linewidth of the reflectance peak is modified.

From all three scenarios in Fig. S4, we also observe that increasing either of the decay rates also increases the linewidth of the reflectance spectrum as the linewidth of an emitter scales proportionally with the total decay rate. In summary, the higher Γ_r is and the lower Γ_{nr} is, the more similar the ML
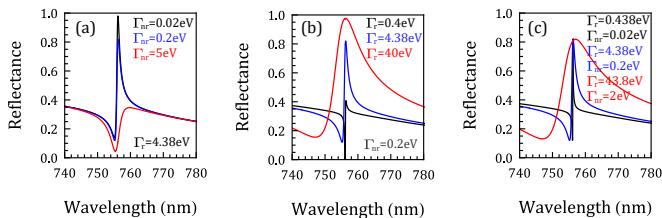
FIG. S4. (a) Reflectance of a monolayer with constant $\Gamma_{\text{r}} = 4.38$ meV, and $\Gamma_{\text{nr}} = 0.02$ meV (black), 0.2 meV (blue), and 5 meV (red). (b) Reflectance of a monolayer with constant $\Gamma_{\text{nr}} = 0.2$ meV, and $\Gamma_{\text{r}} = 0.4$ meV (black), 4.38 meV (blue), and 40 meV (red). (c) Reflectance of an monolayer with constant ratio $\Gamma_{\text{r}}/\Gamma_{\text{nr}}$. $(\Gamma_{\text{nr}}, \Gamma_{\text{nr}}) = (0.438$ meV, 0.02meV) (black), (4.38 meV, 0.2 meV) (blue), (43.8 meV, 2 meV) (red). Both the top and bottom hBN encapsulations are chosen to be 60 nm thick for these simulations.

mirror is to an ideal perfect mirror.

V. SIMULATION OF DIFFERENT CAVITY CONFIGURATIONS

We use TMM and FDTD techniques to simulate different cavity configurations. We start by simulating the reflectance spectrum and the spatial intensity profile when a TMD monolayer mirror is illuminated by a plane wave excitation (Fig. S5). We then simulate the case where two TMD monolayer mirrors are separated by air (Fig. S6). We also calculate the Q-factor and effective mode length for the resulting cavity. After that, we simulate the case of an hBN-TMD heterostructure consisting of two TMD monolayers separated by hBN in the middle and encapsulated by hBN on the top and bottom (Fig. S7). Finally, we simulate the realistic scenario when such a heterostructure is placed on a Si substrate with a 285 nm thick layer of SiO_2 on top (Fig. S8).

The reflectance spectra of the devices are calculated by TMM and the 1D FDTD method, by illuminating the device with a broadband plane wave source and monitoring the reflected light. The cavity field profile, effective mode length, and Q-factor are simulated when exciting the cavity mode with a broadband dipole through FDTD simulations. For effective mode length calculations, we used the definition

$$L_{\text{eff}} = \frac{\left(\int |E|^2 dx\right)^2}{\int |E|^4 dx}, \tag{S3}$$

where the integration is performed over the hBN/TMD/hBN/TMD/hBN heterostructure. This quantity is then a measure of the distribution of the electric field intensity in the nano-cavity. It is equal to the physical thickness of the device for non-resonant wavelengths (constant intensity along the full structure) and becomes reduced if there is a localization of the electromagnetic field.

VI. OPTICAL MODE'S ANGULAR DEPENDENCE

In typical planar cavities, the photonic mode dispersion has a characteristic parabolic dependence. It originates in the dif-

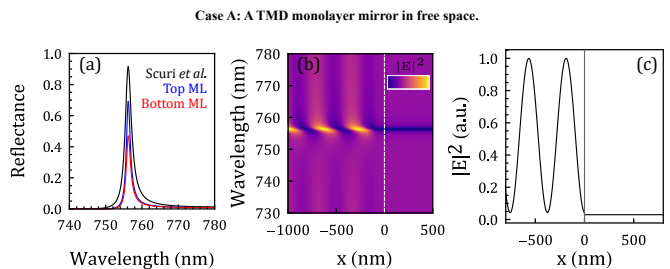Case A: A TMD monolayer mirror in free space.

FIG. S5. (a) Simulated reflectance spectrum of the top (blue), bottom (red), and Scuri *et al.* (black) TMD monolayer (ML) mirror in free space. As expected from a two-level emitter, the incident light is reflected back at the excitonic resonance frequency. (b) Spatial electric field intensity profile $|E|^2$ as a function of wavelength when the TMD (top), located at $x = 0$ nm as marked by a dashed vertical line, is illuminated with a plane wave source from the left. (c) Spatial intensity profile at the excitonic resonance frequency. On the left-hand side of the TMD (top), one can observe standing waves created by the incident and reflected light. The intensity drops on the right-hand side as the TMD reflects the incident light at the resonant frequency.

Case B: Two TMD monolayer mirrors in free space separated by air

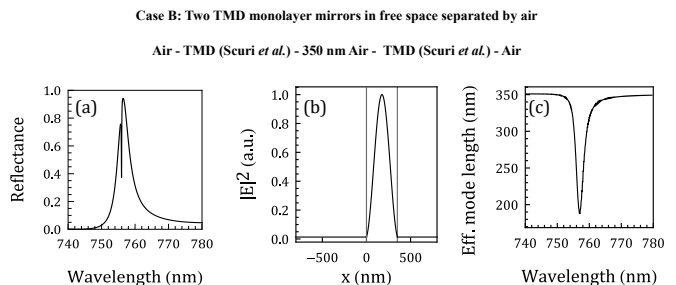Air - TMD (Scuri *et al.*) - 350 nm Air - TMD (Scuri *et al.*) - Air

FIG. S6. (a) Simulated reflectance spectrum when two TMDs (Scuri *et al.*) are separated by 350 nm of air. The dip in the reflectance spectrum at $\lambda \sim 756$ nm indicates the formation of a cavity mode. (b) Spatial intensity profile at the cavity resonance frequency. The TMDs positions are marked by vertical lines. (c) Effective cavity mode length as a function of wavelength. Here the integration is performed over the TMD-air-TMD region. The estimated Q-factor of the cavity is ~ 2828.

ferent phase shifts that the light acquires as it propagates at different angles inside the cavity. Since the phase shift upon a reflection in a DBR or metallic mirror does not have any wavelength dependence, the difference in the acquired phase upon a cavity round-trip depends exclusively on the angle of incidence. A significant difference of the new architecture that we present in this work, comes from the fact that the phase has a strong dependence on the light's wavelength near the resonance of a Lorentz oscillator. A variation in the propagation phase can be compensated by a phase shift induced by a small change in the wavelength. An immediate consequence is the weak dispersion of the cavity mode, as shown in Fig. S9.

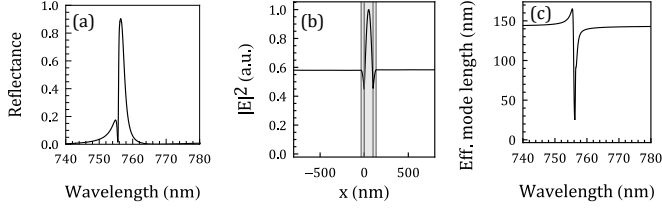**Case C: An hBN-TMD heterostructure cavity in free space**

Air - 35 nm hBN - TMD (Scuri *et al.*) - 100 nm hBN - TMD (Scuri *et al.*) - 35 nm hBN - Air

FIG. S7. (a) Simulated reflectance spectrum for two TMDs (Scuri *et al.*) separated by 100 nm of hBN, and encapsulated by 35 nm of hBN on each side. (b) Spatial intensity profile at the cavity resonance frequency. The shaded region represents the hBN-TMD heterostructure cavity. (c) Effective cavity mode length as a function of wavelength. The estimated Q-factor of the cavity is ~ 1219.

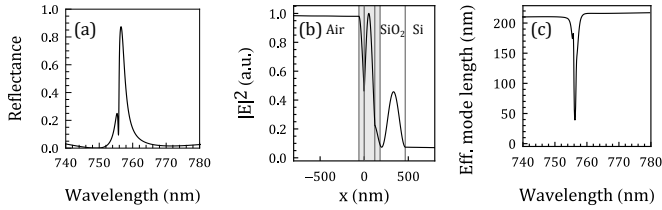**Case D: An hBN-TMD heterostructure cavity on substrate**

Air - 60 nm hBN - TMD (Scuri *et al.*) - 120 nm hBN - TMD (Scuri *et al.*) - 60 nm hBN - 285 nm SiO$_2$ - Si

FIG. S8. (a) Simulated reflectance spectrum of the TMD-hBN heterostructure cavity on a SiO$_2$-Si substrate. (b) Spatial intensity profile at the cavity resonance frequency. The shaded region represents the hBN-TMD heterostructure cavity. (c) Effective cavity mode length as a function of wavelength. The estimated Q-factor of the cavity is ~ 1308.
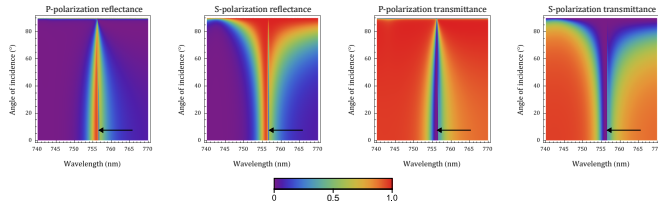

FIG. S9. Calculated reflectance and transmittance for P and S polarized light as a function of the angle of incidence for the configuration of Fig. S6. The black arrows point out the mode for visual guidance. Unlike typical planar cavities the energy of the cavity mode in our device does not change with the angle of incidence. This is a consequence of the excitonic nature of the atomically-thin constituent mirrors.

VII. ADDITIONAL DATA: MAGNETIC FIELD INDUCED CHIRALITY

Due to high spatial inhomogeneity in exfoliated TMDs, the excitonic resonance frequency, Γ_r and Γ_{nr} can vary significantly across different spots on the sample. However, we observe the formation of a cavity, albeit with slightly different resonant energies and Γ_r/Γ_{nr} ratios, across a significant portion of the sample.

We performed additional magnetically induced reflective circular dichroism (CD) measurements over a larger range of magnetic fields in another spot on the sample for comparison of different cavity spots. The magnetic field is varied from -10 T to 10T. Fig. S10b shows the reflective CD measurement results. For the highest applied magnetic field, we obtain a contrast of > 1 in the CD, which is larger than our measurement in the original sample spot. From the magnetically induced energy splitting of the chiral modes ΔE of the cavity we extract a g-factor of $g = -4.40 \pm 0.12$ (panel c), using the relationship $\Delta E = g\mu_B B$, where μ_B is the Bohr magneton and B is the magnetic field strength. The obtained value is in good agreement with the reported value in the main text (and in the literature).
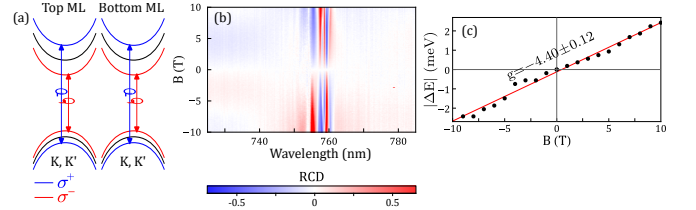

FIG. S10. (a) Schematic showing the Zeeman splitting in top and bottom monolayers. This gives rise to the two chiral modes of the cavity with σ^+ and σ^- polarizations. (b) RCD of the heterostructure cavity for increasing B at a different spot. (c) Energy difference ΔE between the σ^+ and σ^- cavity modes as a function of B. From a linear regression, we extract a magnetic factor $g = 4.40 \pm 0.12$